Received: 20 October 2021 | Revised: 13 August 2022 | Accepted: 23 September 2022

DOI: 10.33012/navi.567

ORIGINAL ARTICLE

Resilient Smartphone Positioning Using Native Sensors and PPP Augmentation

Sihan Yang | **Ding Yi*** | **Sudha Vana** | **Sunil Bisnath**

Department of Earth and Space Science, Lassonde School of Engineering, York University, Toronto, Ontario, Canada

Correspondence
Ding Yi
Department of Earth and Space Science, Lassonde School of Engineering, York University, Toronto, Ontario, Canada
Email: dingyi@yorku.ca

Abstract

With the ubiquitous use of global navigation satellite system (GNSS) receivers, navigation solutions from smartphones have become integrated in various applications throughout our lives. These ultra-low-cost GNSS receivers have the drawbacks of insufficient observations and poorer signal reception quality than higher-cost receivers. Since 2016, smartphones using the Android operating system have been able to output raw GNSS pseudorange and carrier-phase measurements, thereby enabling improved navigation capabilities. The realm of sensor fusion is also being explored by using smartphone sensors, including inertial measurement units (IMUs), cameras, and other fusion techniques. The research presented herein deployed only IMU and GNSS sensors native to existing smartphones and achieved a standalone solution using PPP/IMU integration that outperformed standard techniques. In open-sky vehicle experiments, the sensor integration algorithm achieved 1.6-m horizontal RMS, thus reducing 80% of horizontal errors in GNSS-challenging environments through a tightly coupled GNSS-PPP solution that is yet to appear in publications.

Keywords

sensor fusion, smartphone GNSS, smartphone PPP, urban positioning

1 | INTRODUCTION

Navigation solutions from smartphones and other smart devices equipped with GNSS and other sensors have become an integral part of our daily lives, and support growing industries such as shared economy, advanced driver-assistance systems (Dumitru et al., 2018), and the Internet of things (Bilal, 2017). Rapidly evolving user technologies that are enabled by, or benefit from, location and timing information are advancing the GNSS industry, and more robust positioning, navigation, and timing (PNT) solutions are actively being pursued. Of the more than 6 billion consumer-grade GNSS receivers (approximately 10 USD) in use, more than 90% are installed on cellphones (EUSPA, 2019). This proliferation of consumer-grade PNT information for individual users not only allows more technologies to be used in daily life but also has worldwide influence by providing a crucial source of

information for big-data services. Given the large amount of information available from every smartphone, humans' lives can be improved; for example, smart city services and planning are already being undertaken. These advances require the research community to increase the performance robustness of smartphone PNT solutions, and increase resilience in obstructed environments.

From this viewpoint, traditional GNSS point-positioning solutions from smartphones have substantial limitations because of the poor performance of ultra-low-cost antennas and chips, performance degradation in urban environments, and inherent unavailability in areas lacking GNSS (Farrell & Barth, 1999; Paziewski, 2020; Shinghal & Bisnath, 2021). However, smartphones are now also equipped with more sensors for potential integrated solutions. Among them are accelerometers and gyroscopes using micro-electromechanical system technology forming an inertial measurement unit (inertial measurement unit (IMU; Godha, 2006; Vana et al., 2019; Yang et al., 2014). These sensors native to current smartphones are ideal for improving PNT performance, because the measurements from IMUs are acquired passively, and no further costs are required for smartphone manufacturers, who are already struggling with cost control. This research presents a native sensor fusion for smartphones that combines the precise-point-positioning (PPP) technique (Zumberge et al., 1997) for GNSS and internal IMUs. PPP was selected because it is a more standalone solution than relative techniques such as real-time kinematics (RTKs; Bisnath & Gao, 2009; Eckl et al., 2001). It requires only the connectivity already prevalent in smartphones, and does not require additional local infrastructures to be built or maintained.

Generally, PPP algorithms can be classified into two broad categories depending on how ionospheric delays, one of the major error sources in PPP, are addressed. First, by forming a linear combination of observations at different frequencies, this combined strategy is able to eliminate the ionospheric delays in the estimation and has become commonly adopted in recent decades (Cai & Gao, 2007; Ge et al., 2012; Kouba & Héroux, 2001). However, combined PPP increases the measurement noise, and external ionospheric information cannot be applied (Liu et al., 2017; Xiang et al., 2017). As an alternative, the uncombined mode directly using raw measurements has recently received considerable attention in the PPP community. Owing to the increasing number of International GNSS Service (IGS) stations, accurate products for spatial and temporal ionospheric delays are available through either postprocessing or real-time services. In 2002, Øvstedal (2002) suggested using global ionospheric maps (GIMs; Schaer et al., 1998) with inherent errors of approximately 2–8 total electron content units (Hernández-Pajares et al., 2009) as prior information to correct ionospheric errors when single-frequency GNSS observations are used. Shi et al. (2012) have proposed a refined ionospheric model to further improve single-frequency PPP. In this context, PPP with ionospheric constraints (ICs) has successfully shortened convergence time and improved positioning accuracy for both single- and dual-frequency PPP processing (Gao et al., 2017; Lou et al., 2016; Tu et al., 2013; Zhang et al., 2013). More recently, PPP-IC has been used not only for geodetic surveying but also for low-cost (Nie et al., 2020) and smartphone receivers (Banville et al., 2019; Wang et al., 2021). Furthermore, Yi et al. (2021) have verified that PPP-IC provides more help for smartphones than low-cost and geodetic-grade receivers, and a 72% improvement has been reported in reducing smartphone horizontal root-mean-square error in suburban environments.

Smartphone GNSS receivers are considered ultra-low-cost and have drawbacks of poor measurement quality and other issues (Li & Geng, 2019; Shinghal & Bisnath, 2020). The research community's progress in exploring smartphone-integrated navigation has occurred in step with hardware and software platform development. In the past few years, smartphones have increasingly been equipped with multi-constellation, multi-frequency GNSS hardware. On the software platform side, Google has made raw GNSS readings possible through its application programming interface from 2016, thus allowing researchers to produce their own navigation solutions from raw measurements (Sunkevic, 2017). Since then, phone navigation improvements have become much easier for researchers (Fortunato et al., 2019; Humphreys et al., 2016; Robustelli et al., 2019), thereby enabling the PPP technique to be used as both pseudorange and carrier-phase observables become available (Aggrey et al., 2020; Paziewski, 2020; Wang et al., 2021). Studies in the literature have examined the IMU performance of smartphones. For example, Gikas and Perakis (2016) have investigated a loosely coupled GNSS/IMU solution using older phones from 2012–2013 for intelligent transport system purposes, using a similar phone-on-top setup to that in our experiment. The standard deviation of horizontal errors has been shown to be several meters for both tested phones but degrade by a few more meters in obstructed environments. Yan et al. (2019, 2020) have studied a recent Xiaomi Mi 8 compared with commercial IMUs by using a slower-moving tricycle and tested outage performance by using a modified Kalman filter. The solution showed improvement in GNSS outages, but the solution drifted away meters from the track before any turning movement from the vehicle.

Despite this progress, the specific software/hardware combination of smartphone GNSS-PPP and IMU has received little attention. With a robust GNSS solution from PPP, an enhanced native GNSS-only solution is expected. The novelty of this work is the presentation of new results and analysis using native GNSS and IMUs from a smartphone together with PPP augmentation in realistic driving scenarios with real-world outages. Therefore, the major contributions of this research are to answer the following questions: (a) How does the performance of a smartphone PPP/IMU integrated solutions compare to that of a smartphone using an identical GNSS source but better IMUs? (b) In what scenarios does a smartphone IMU improve navigation solutions, and by how much?

The article is organized as follows: Section 2 explains the PPP-IC model, followed by smartphone IMU preprocessing strategies, the tightly coupled integration Kalman filter, and York PPP engine settings. Section 3 describes the field data collection in suburban driving scenarios. Three solutions involving different GNSS/IMU combinations are analyzed in Section 4. Section 4 also analyzes the outage performance from the integrated solutions. Section 5 and Section 6 discuss the answers to the research questions and envision future work that may extend this research.

2 | METHODS AND DATA PROCESSING STRATEGIES

This section begins with the technique of PPP-IC constrained by GIM information, including the carrier-to-noise ratio (C / N_0) weighting scheme adopted in this study. Details regarding smartphone IMU raw data preprocessing and tightly coupled PPP/IMU integration, as well as the York PPP engine settings are introduced subsequently.

2.1 | Dual-Frequency PPP-IC Model

PPP uses GNSS pseudorange and carrier-phase observations, along with precise satellite products, to achieve high-accuracy location-based services for users with standalone receivers. The uncombined PPP observation equations are expressed as follows:

$$\begin{aligned} P_{u,i}^{s} &= \rho_{u,i}^{s} + c\left(dt_u - dt^s\right) + T_u^s + \gamma_i I_{u,1}^s + b_{u,P_i} - b_{P_i}^s + \varepsilon_{P_i} \\ L_{u,i}^{s} &= \rho_{u,i}^{s} + c\left(dt_u - dt^s\right) + T_u^s - \gamma_i I_{u,1}^s + b_{u,L_i} - b_{L_i}^s \\ &\quad + \lambda_i N_i^s + \varepsilon_{L_i} \end{aligned} \tag{1}$$

where $\rho_{u,i}^{s}$ refers to the geometric distance between satellite s and user receiver u; $P_{u,i}^{s}$ and $L_{u,i}^{s}$ are, respectively, the observed pseudorange and carrier-phase measurements on frequency i $(i \in \{1,2\})$; c is the speed of light in a vacuum; dt_u and dt^s represent receiver and satellite clock offsets, respectively; T_r^u is the slant troposphere delay, and $\gamma_i = \frac{f_1^2}{f_i^2}$ is the coefficient that converts the first-frequency slant ionospheric delay $I_{r,1}^u$ on frequency i. $b_{u,P}$ and $b_{u,L}$ are code and phase biases at the receiver end, respectively; similarly, b_P^s and b_L^s are the code and phase biases at the satellite end, respectively; λ_i denotes the carrier wavelength in length at i frequency, and N^s is the unknown float ambiguity; and ε_P and ε_L are the measurement noise of pseudorange and the carrier phase, respectively. To prevent the receiver differential code bias (DCB) from being incorporated into estimated slant ionospheric delay, Xiang and Gao (2017) and Xiang et al. (2017) have proposed to preserve the slant ionospheric refraction and receiver DCB terms in PPP-IC processing. The previously stated Equation (1) can be rewritten as:

$$\begin{aligned} P_{u,i}^{s} &= \rho_{u,i}^{s} + (cdt_u + b_{u,P_3}) + T_u^s + \gamma_i (I_{u,i}^{s,constrained} - \frac{1}{\gamma_i - 1} DCB_u) \\ &\quad + \varepsilon_{P_i} \\ L_{u,i}^{s} &= \rho_{u,i}^{s} + (cdt_u + b_{u,P_3}) + T_u^s - \gamma_i (I_{u,i}^{s,constrained} - \frac{1}{\gamma_i - 1} DCB_u) \\ &\quad + \lambda_i \tilde{N}_{u,i}^{s} + \varepsilon_{L_i} \end{aligned} \tag{2}$$

where b_{u,P_3} is the receiver code bias calculated by ionospheric-free combinations, and $\tilde{N}_{u,i}$ is the estimated carrier-phase ambiguity, coupling with code and phase biases. DCB_u denotes the estimated receiver DCB, and $I_{u,i}^{s,constrained}$ is the estimated ionospheric error constrained by the GIM information. For simplicity, we use the term *PPP* instead of *PPP-IC* to describe the processing strategies in the following sections.

The measurement weighting scheme also plays a crucial role in determining the user's position. Traditionally, the satellite-elevation-based weighting scheme is widely used in PPP processing (Eueler & Goad, 1991). However, the very inexpensive smartphone linearly polarized antenna collects GNSS signals from all directions and is consequently susceptible to multipath effects. Recently, multiple studies (Banville et al., 2019; Shinghal & Bisnath, 2021; X. Zhang et al., 2018) have demonstrated that the carrier-to-noise ratios are more appropriate than satellite elevation angles to serve as the weighting indicator, because the multipath affected signals usually have lower values of C/N_0. Therefore, this study used the

C/N_0-based weighting strategy, and the standard deviation of the pseudorange measurement σ was estimated as (Banville et al., 2019; Shinghal & Bisnath, 2021):

$$\sigma = a + b \times 10^{-\frac{1}{2} \times \frac{C/N_0}{10}} \tag{3}$$

where a and b are constant coefficients that are determined empirically.

2.2 | Smartphone IMU Raw-Data Preprocessing

Smartphone IMU measurements were collected by using the GnssLogger application v3.0.0.10 developed by Google. This application is able to record raw IMU and GNSS measurements in a text file for postprocessing. To synchronize with GNSS timestamps, we used the UTCTimeMillis file logged by the application with GNSS timestamps of the same label. The uncalibrated raw IMU measurements were used because the bias from the accelerometer and gyroscope is dynamically estimated from the extended Kalman filter. Android smartphones do not share the same default body axes as our Xsens MTi-7 IMU in its motion frame. To adapt the smartphone IMU output to the navigation engine programmed in the north-east-up (NEU) frame, we first performed a frame transformation. As shown in Figure 1(a), the IMU coordinate system is converted to a vehicle body coordinate system. Table 1 describes the intuition behind the readings along the *x*-, *y*-, and *z*-axes for the accelerometer and gyroscope.

All raw IMU measurements were preprocessed further by re-sampling to 100 Hz with MATLAB's built-in functions in interpolation mode. Three reasons led to the re-sampling decision: (a) as demonstrated in Figure 1(b), the accelerometer and gyroscope readings were not synchronized over the sampled 0.25 s, showing separate timestamps, in contrast to conventional IMUs; (b) the IMU raw measurements were not spaced equally, because the time gaps between measurements were not constant (Figure 2); and (c) by setting up a uniform data rate, the same integrated filter solution can be compared between the commercial low-cost Xsens and the smartphone without additional processing.

The preprocessing was performed to ensure that the two IMUs were processed in the same frame and re-sampled to 100 Hz. Figure 3 presents the comparison of IMU raw measurements between the Xsens IMU (green) and Xiaomi Mi 8 IMU (blue). The Xsens MTi-7 low-cost IMU is used as a comparison. The low-cost IMU does not provide an ideal truth as reference. However, the matching pattern over all measurements and axes for Mi 8 against Xsens MTi-7 showed promising performance of the integrated solution.

Figure 3 presents some context for the subsequent data processing and positioning performance during GNSS outages in particular. Acceleration along the *y*-axis is at the same order of magnitude as that along the *x*- and *z*-axes. The observation is not intuitive, because the *y*-axis is orthogonal to the vehicle's direction of travel. One possible explanation is the vibration from vehicle movements during the road tests.

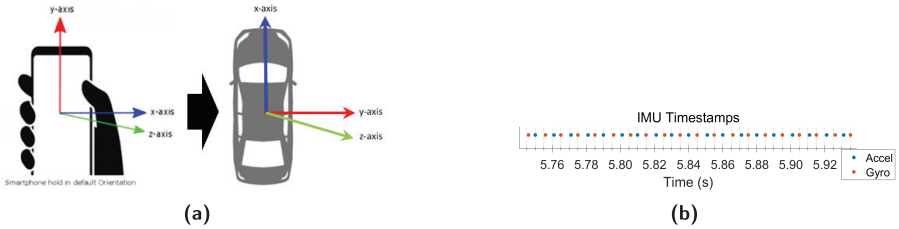

FIGURE 1 Characteristics of smartphone IMU measurements: (a) depicts the transformation to a conventional frame, while (b) depicts a snapshot of IMY timestamps over 0.25 s.

TABLE 1
Explanation of IMU Axes

Axis/ measurements	Accelerometer	Gyroscope
X	Direction of travel	Roll
Y	Lateral	Pitch
Z	Vertical	Yaw

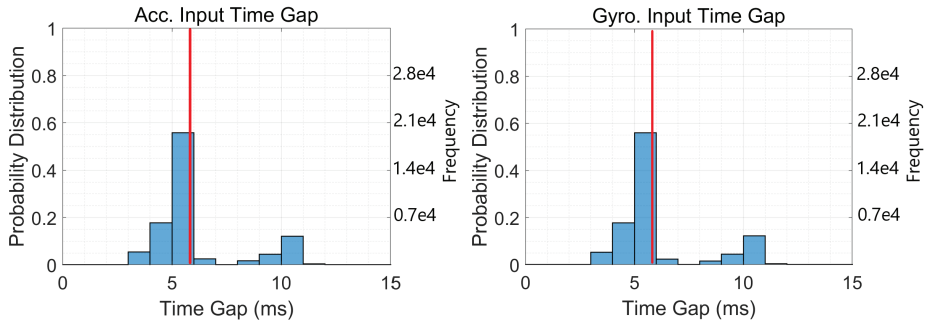

FIGURE 2 Histograms of time gaps between IMU measurements; the red line indicates a mean time gap of 5.8 ms.

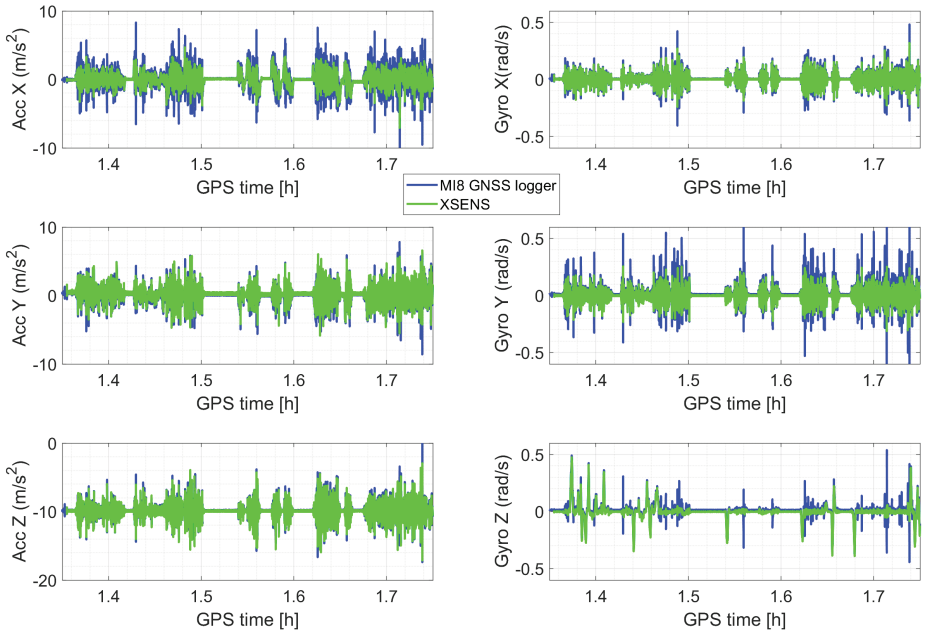

FIGURE 3 Raw IMU measurements: Mi 8 vs. Xsens MTi-7

2.3 | Tightly Coupled PPP/IMU Integration

This study used a tightly coupled approach for combining smartphone IMU and GNSS measurements. Compared with a loosely coupled approach, a tightly coupled integration incorporates GNSS raw measurements of pseudoranges and the carrier phase into the extended Kalman filter rather than processing velocity and position states from a separate GNSS filter and IMU mechanization. The access to raw GNSS measurements and IMU measurements using the Android application

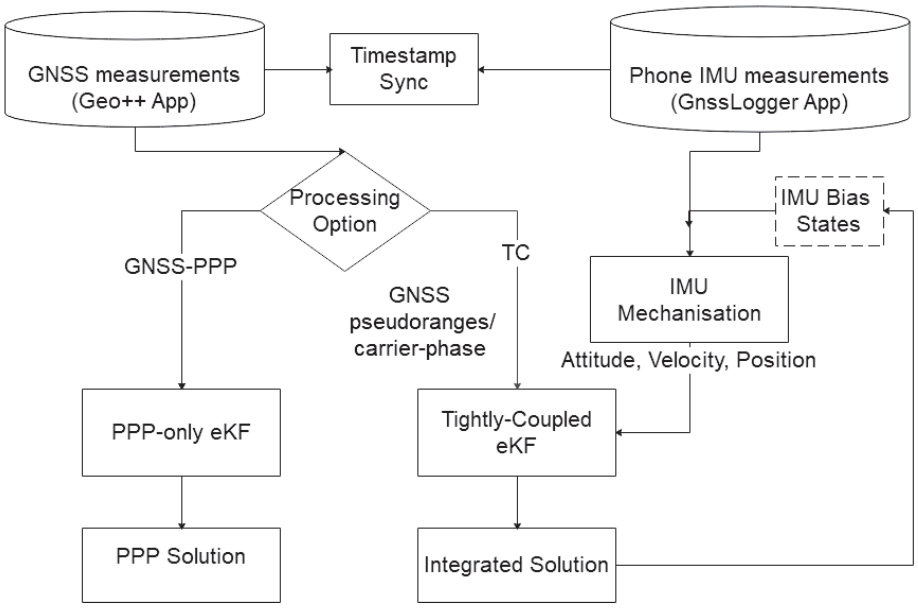

FIGURE 4 Tightly coupled GNSS-PPP integration architecture

programming interface allows for a tightly coupled solution to be computed. Furthermore, we aimed to investigate the outage performance of the GNSS-PPP/IMU integration; a tightly coupled approach enabled generation of a navigation solution when only two or three satellites were available. The architecture of the tightly coupled integration is shown in Figure 4.

Raw GNSS measurements were collected by using the Geo++ 2.1.6 application in Receiver Independent Exchange (RINEX) format, because some software issues were experienced with Google's GnssLogger application with RINEX recording. Two types of measurements were used: the pseudoranges, $P^s_{u,i}$, and carrier-phase, $L^s_{u,i}$, observations. IMU measurements were recorded with the GnssLogger application, as explained in earlier sections. Uncalibrated raw IMU measurements were used, with feedback received from bias estimation computed from the last Kalman filter epoch at the beginning of each mechanization epoch. The measurements used were specific forces f^b_{ib} and angular rate ω^b_{ib}, where the superscripts and subscripts indicate that the terms were measured in the IMU body frame with respect to the inertial frame and resolved around the IMU body frame. The timestamp synchronizer function matched the IMU epochs with GNSS epochs. As the GNSS measurement was collected at 1 Hz, the 100-Hz IMU measurements ran the mechanization process 100 times between each available GNSS epoch. The mechanization equations produce attitude, ε_{imu}, velocity, v_{imu}, and a position, p_{imu}, estimation for each tightly coupled filter epoch k. The navigation states vector is defined as:

$$\delta X_{nav,k} = \begin{bmatrix} \delta p_k & \delta v_k & \delta \varepsilon_k \end{bmatrix}^T \tag{4}$$

where each term is a 3×1 vector for each of the x-, y-, and z-axes. For the IMU, two additional bias states were estimated: bias in accelerometer b_a and in gyroscope b_g. For each IMU epoch j, the two estimated bias terms were fed back to the beginning of the next mechanization stage additively to generate input f_b and ω_b to the mechanization equations. Both bias estimates were initialized to zero.

$$\delta f_{b,j} = f^b_{ib,j} + b_{a,j-1} \qquad \delta \omega_{b,j} = \omega^b_{ib,j} + b_{g,j-1} \tag{5}$$

The design matrix H maps the measurement innovation vector, dz, to each estimated state through their partial derivatives. In the tightly coupled approach, our measurement innovation dz, is defined as the differences between the observed GNSS pseudorange/carrier-phase measurements and the modeled values.

$$dz = \begin{bmatrix} P^s_{GNSS,i} - P^s_{TC,i} \\ \cdots \\ L^s_{GNSS,i} - L^s_{TC,i} \\ \cdots \end{bmatrix}$$

The design matrix **H** is defined as:

$$H = \begin{bmatrix} \frac{\partial P^s_{GNSS,i}}{\partial x} & \frac{\partial P^s_{GNSS,i}}{\partial y} & \frac{\partial P^s_{GNSS,i}}{\partial z} & 0_{1\times3} & 0_{1\times3} & \frac{\partial P^s_{GNSS,i}}{\partial zpd} & 1 & 0_{1\times3} & 0_{1\times3} & 0\ldots \\ & & & \cdots & \cdots & & & & & \\ \frac{\partial L^s_{GNSS,i}}{\partial x} & \frac{\partial L^s_{GNSS,i}}{\partial y} & \frac{\partial L^s_{GNSS,i}}{\partial z} & 0_{1\times3} & 0_{1\times3} & \frac{\partial L^s_{GNSS,i}}{\partial zpd} & 1 & 0_{1\times3} & 0_{1\times3} & \lambda\ldots \\ & & & \cdots & \cdots & & & & & \end{bmatrix} \quad (6)$$

From left to right, the terms each relate to one of the estimated state: position in x, y, and z, velocity, attitude, wet tropospheric errors, receiver clock bias and drift, bias in accelerometer/gyroscope, and float ambiguities. Details of the GNSS-PPP states and sensor fusion combinations are given in the next section.

2.4 | York PPP Engine Settings

In the user software domain, York University's York-PPP engine is used to generate smartphone tightly coupled PPP/IMU solutions (Aggrey et al., 2020). Table 2 highlights the products and tuned parameters used for obtaining the corresponding results.

The dual-frequency observations collected by a Xiaomi Mi 8 smartphone were processed in PPP-IC mode. PPP uses a series of estimations of precise corrections to improve solution sub-meter-level accuracy. We used the GeoForschungsZentrum (GFZ) rapid products as a precise correction to mitigate satellite orbit and clock errors, and satellite DCBs were corrected by using the products from the Chinese Academy of Sciences. Meanwhile, the tropospheric delays consisting of hydrostatic (dry) and wet components were estimated through global mapping function (GMF) modeling and a random walk with white noise, respectively. Of note, the accuracy of the geospatial information modeling (GIM) products vary among IGS Analysis

TABLE 2
York PPP Engine Settings for Smartphone Tightly Coupled PPP/IMU

PPP/IMU TC settings	Products and parameters
Orbit and clock corrections	GFZ rapid products
DCB	CAS products
Tropospheric delays	Hydrostatic: GMF modeling Wet: estimated
GIM	Combined final IGSG products
Standard deviation of pseudorange (m)	4
Standard deviation of carrier phase (m)	0.06

Center Coordinators (IACCs), and sometimes the GIM root-mean-square-error maps cannot serve as a good indicator for the stochastic model (Zhao et al., 2021). Therefore we selected the combined final IGSG GIM products and amplified the GIM standard deviations in case of unknown GIM inherent errors. The following parameters, such as standard deviations of pseudorange and carrier-phase smartphone measurements, were derived from postprocessing calculations, and observations with post-fit residuals tenfold larger than those empirical standard deviations considered as outliers and rejected automatically by the York-PPP engine.

3 | DATA COLLECTION

A field experiment was designed to produce and analyze the smartphone GNSS-PPP/IMU integrated solution. Figure 5 shows the experimental setup. The experimental vehicle (Figure 5[a]) was taken to suburban Toronto on DOY 211 of 2021 for a road test lasting approximately 25 min. Meanwhile, in a customized wooden box, various GNSS antennas and receivers were fixed onto the surface, as well as a low-cost industrial-grade Xsens MTi-7 IMU. The setup is shown in Figure 5(b). Both the smartphone and the NovAtel NOV850 antenna were placed on the top of the box. The phone was placed in a silicon shell attached to the surface of the wooden box, facing up. Its direction was oriented so that the phone's *y*-axis pointed toward the direction of travel, and the *z*-axis faced upward. This placement was designed to maintain a consistent and orthogonal direction of travel, so that the IMU body frame remained stationary with respect to the vehicle frame. Furthermore, real-time kinematic tightly coupled positioning (RTK/TC) integrated results were generated from a pair of NovAtel PwrPak 7 SPAN geodetic receivers with the base station on a rooftop within 5 km of the vehicle trajectory. Its coordinates were computed beforehand by using 24-hour PPP processing. All reference solutions were computed with Inertial Explorer (v8.90.4806) software from NovAtel.

One possible concern is that, although the car was driven in a real-world scenario, the phone was not placed in a location that users would actually choose. The reasons for the experimental design were that (a) in the vehicle, the phone experiences GNSS signal blockage and degradation, and (b) if the phone is not fixed onto a surface, the phone's stance can change during the data collection, and the IMU behavior to acceleration or vibration would not be comparable to that of the fixed conventional IMU. The research goals were to perform a study to understand the smartphone-integrated PPP solution under optimal conditions closest to ideal driving scenarios for smartphones. The approach also allowed for fair raw-measurement comparison between the IMUs. Therefore, the experiment was designed to enable control over variables.

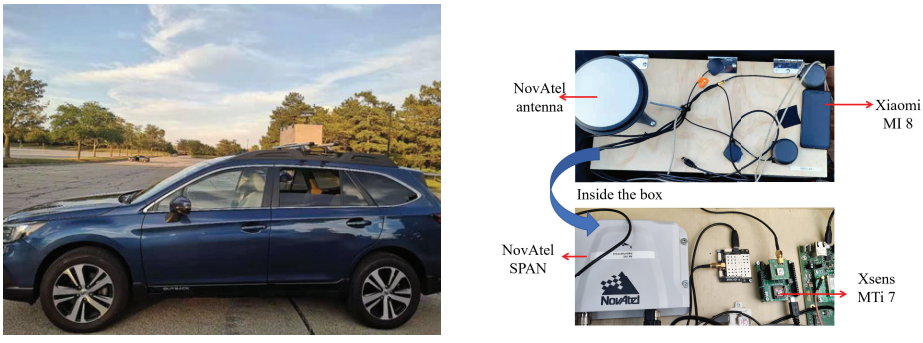

FIGURE 5 (a) depicts the experimental vehicle while (b) depicts the experimental setup.

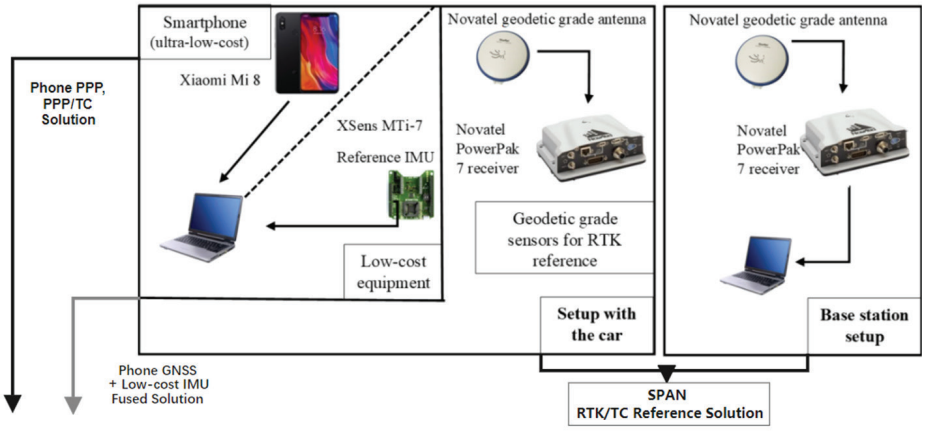

FIGURE 6 Experimental flowchart

An experimental flowchart of the experiment is shown in Figure 6. The commercial Xsens IMU was placed alongside the Xiaomi Mi 8 smartphone as a reference to compare raw inertial measurements. Three solutions were generated from the setup: the phone GNSS-only PPP solution, its integrated solution using native IMUs, and its integrated solution using the Xsens MTi-7 IMU. These solutions allowed us to analyze the performance of the GNSS-only PPP solution versus any integrated solution, as well as to compare the two integrated solutions using identical GNSS measurements but different grades of IMU.

4 | RESULTS AND ANALYSIS

To answer the proposed research questions, we compared the raw IMU measurements between smartphone-grade IMU and Xsens. Two specific scenarios, the open-sky environments and underpass environments, were chosen to be analyzed in detail. In an underpass environment, the GNSS receiver experiences partial or complete outage for several epochs, depending on the size of the underpass.

4.1 | Assessing Kinematic Positioning and Outage Performance

Figure 7(a) displays the overall aerial view of trajectory in Google Earth. The travel directions and the start/end point are marked by yellow arrows and a red dot, respectively. The corresponding overall horizontal errors are illustrated in Figure 7(b), wherein the horizontal errors processed by dual-frequency PPP-only, and dual-frequency tightly coupled PPP with the Mi 8 IMU and with Xsens IMU, are represented as the red, blue, and green lines, respectively. The errors are computed on an epoch-by-epoch basis by using the Synchronized Position Attitude Navigation (SPAN) reference trajectory. Owing to the signal blockage in the GNSS-challenging underpass environments, two error peaks were observed at elapsed times of approximately 6 and 19.5 min without the external information from the IMU (red line), and these two underpasses are marked by red ovals in Figure 7(a).

To better study the positioning benefits from using an IMU, Table 3 highlights the horizontal root mean square (RMS) with different percentiles, and several notable improvements are achieved. First, a significant level of improvement was observed

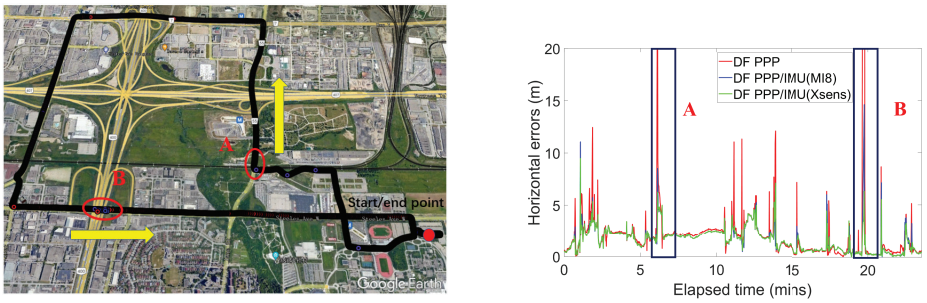

(a) (b)

FIGURE 7 Aerial view of vehicle trajectories and corresponding overall horizontal error comparison for all sensor fusion combinations: (a) depicts an aerial view of the vehicle trajectories from Google Earth while (b) depicts the overall horizontal error comparison for different sensor fusion combinations.

TABLE 3
Overall Horizontal RMS with Different Sensor Fusion Combinations

Sensor combinations	DF-PPP	DF-PPP/IMU (MI 8)	DF-PPP/IMU (XSens)
68th percentile rms (m)	1.3	1.2	1.2
95th percentile rms (m)	1.9	1.7	1.7
100th percentile rms (m)	5.2	2.1	1.9

by integrating IMU sensors: the overall horizontal RMS decreased from 5.2 m to 2.1 m with the help of the Mi 8 IMU, and further decreased to 1.9 m after replacement with the Xsens IMU. In contrast, the improvements from using IMU measurements decreased to 0.2 m (95th percentile RMS) and 0.1 m (68th percentile RMS) after filtering of the outliers from the underpass environments, thus indicating that the improvement from tightly coupled PPP/IMU integration is highly relevant to scenarios with obstructions. To study the effects of IMUs on GNSS-denied scenarios, we selected two specific portions of the trajectory, Underpass A and Underpass B, for the following analysis.

4.1.1 | *Underpass A*

The first underpass scenario was a short turn under a railway bridge, as shown in Figure 8(a). Figure 8(b) illustrates four trajectories in underpass A, where the referenced NovAtel SPAN RTK/TC solutions and standalone dual-frequency PPP solutions are represented by purple and red dots, respectively, and the tightly coupled, dual-frequency PPP with the Mi 8 IMU and Xsens IMU are presented in blue and green dots, respectively.

Figure 9(a) presents the time series of horizontal errors processed by the three aforementioned sensor combinations around Underpass A (5–7 min). Owing to the GNSS signal outages, the horizontal errors were expected to increase rapidly and reach a maximum when passing through Underpass A (elapsed time at 6.1 min). Correspondingly, a positive correlation was observed between the horizontal errors and the position dilution of precision (PDOP) values through the comparison of Figure 9(a) and Figure 9(b). The PDOP values above 20 are not

FIGURE 8 Photograph and aerial view of trajectory for Underpass A: (a) depicts a Google Earth view of Underpass A while (b) depicts Google Earth trajectories for three sensor fusion combinations.

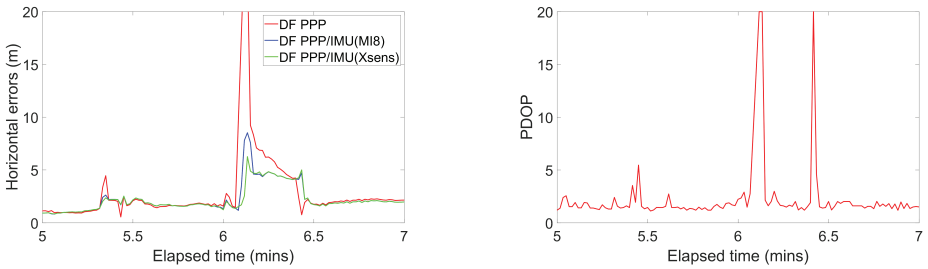

FIGURE 9 Time series of horizontal errors and PDOP values for elapsed times between 5 and 7 min for Underpass A: (a) depicts the time series of horizontal errors and (b) depicts the time series of PDOP values.

shown, because they indicated no or extremely poor GNSS geometry. A high PDOP value was also observed when the elapsed time reached 6.4 min, mainly because of GNSS signal blockage from the passing trucks and vans. Of note, by integrating IMU sensors, an obvious trend was observed of decreasing horizontal errors under the underpass environments, e.g., the horizontal error peak of dual-frequency GNSS PPP-only solutions significantly decreased from 26.1 m to 8.5 m (Mi 8 IMU) and 6.3 m (Xsens IMU).

Table 4 highlights the horizontal RMS with different levels of percentiles when the elapsed times were between 5 and 7 min. In contrast to that of dual-frequency PPP solutions, the overall RMS of integrating IMUs decreased from 4.3 m to 2.7 m (Mi 8 IMU) and 2.5 m (Xsens IMU), thus leading to 37% and 42% accuracy improvements for smartphone positioning under such a GNSS-challenging environment. Meanwhile, further 95th and 68th percentile RMS analysis indicated that, by screening those epochs, which might have been affected by GNSS signal blockage, poor GNSS geometry, as well as multipath effects, the IMUs would be less beneficial in improving solution accuracy but showed no negative impacts.

4.1.2 | *Underpass B*

For Underpass B, compared with Underpass A, the second outage was more challenging for the smartphone positioning, because it was approximately 100-m long under three consecutive highway ramps (Figure 10[a]), thus causing intermittent GNSS signal availability. As shown in Figure 10(b), the dual-frequency PPP solution (red dots) showed decreased accuracy when the vehicle was passing under

TABLE 4
Horizontal RMS with Different Sensor Fusion Combinations for Elapsed Times Between 5 and 7 min (Underpass A)

Sensor combinations	DF-PPP	DF-PPP/IMU (Mi 8)	DF-PPP/IMU (Xsens)
68th percentile RMS (m)	1.7	1.6	1.6
95th percentile RMS (m)	2.5	2.3	2.2
100th percentile RMS (m)	4.3	2.7	2.5

(a) (b)

FIGURE 10 Photograph and aerial view of trajectory for Underpass B: (a) is a Google Earth view of the underpass and (b) is a Google Earth view of the trajectories for the three sensor fusion strategies.

Underpass B, thus leading to only one positioning solution that overlapped with another highway ramp during the GNSS outage. In contrast, the PPP integrated Xsens IMU solutions were able to provide continuous dead reckoning, because the blue dots were almost in line with the center line of the road and referenced trajectories. Interestingly, in terms of the tightly coupled PPP integrated with Mi 8 IMU solutions (blue dots), the IMU mechanization results were reliable at the beginning of the outage but drifted rapidly after a few seconds, and reached a maximum horizontal error of 15 m for Mi 8 native IMU, and approximately 6 m for Xsens MTi-7. This finding was expected, given the limitations of the smartphone-grade hardware.

Figure 11(a) and Table 5 highlight the time series of horizontal errors and RMS with different percentiles across Underpass B. Through comparison of Figure 11(a) and 11(b), a correlation between horizontal errors and satellite geometry was observed. The statistics notably indicated that the overall RMS decreased from 15.9 m to 2.5 m with incorporation of the smartphone IMU, and was as low as 1.2 m after replacement with the commercial Xsens IMU. Meanwhile, both the 95th and 68th percentile RMS values indicated that the IMU offered only slight gains for smartphone positioning in more open-sky environments: More than 96.2% of the epochs had more than four satellites. Together, these results suggested that, with the aid of IMU measurements, smartphone positioning becomes more resilient to signal-blockage-prone environments, in that the positioning accuracy was significantly improved in areas with poor GNSS geometry, and the fusion also was not detrimental to PPP solutions with sufficient satellite visibility. In contrast, positive impacts were observed from the ultra-low-cost smartphone IMU, with comparable tightly coupled positioning performance with respect to that of the commercial IMU, despite their hardware discrepancy, thus showing great potential in future smartphone location-based services.

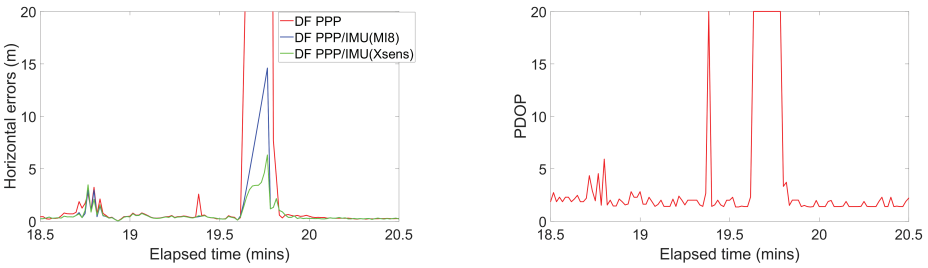

FIGURE 11 Time series of horizontal errors and PDOP values for times between 5 and 7 min for Underpass B: (a) depicts the time series of horizontal errors and (b) depicts the time series of PDOP values.

TABLE 5
Horizontal RMS Using Different Sensor Fusion Combinations for Elapsed Time Between 18.5 and 20.5 min (Underpass B)

Sensor combinations	DF-PPP	DF-PPP/IMU (Mi 8)	DF-PPP/IMU (Xsens)
68th percentile RMS (m)	0.3	0.3	0.3
95th percentile RMS (m)	0.8	0.8	0.7
100th percentile RMS (m)	15.9	2.5	1.2

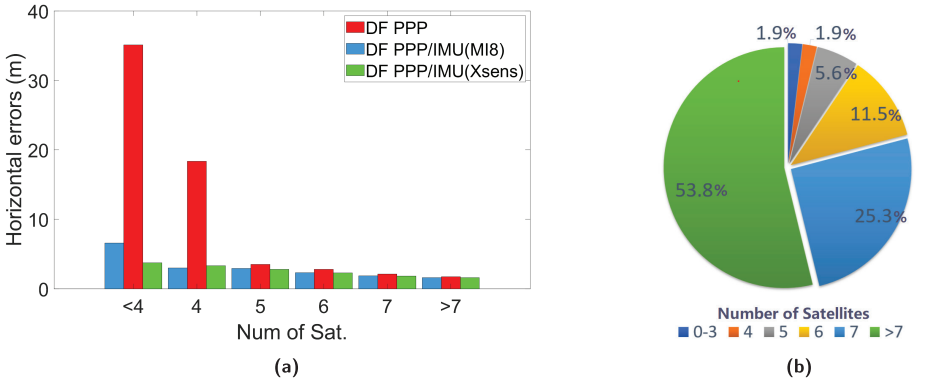

FIGURE 12 Overview of satellite availability and corresponding accuracy improvement: (a) depicts solution improvement via number of visible satellites while (b) depicts the percentage of satellites processed.

4.2 | Identifying Scenarios in Which Sensor Fusion Benefits Most

Figure 12(a) presents the horizontal RMS bars with visible satellites. Owing to the satellite geometry, smartphone positioning accuracy increases with the growing number of satellites for these three sensor fusion combinations. In addition, as summarized in Figure 12(b), although more than half the epochs involved observations from more than seven satellites, it was the 3.8% epochs with only zero to four satellites that decreased the overall positioning performance. In these GNSS-challenging scenarios, an accuracy improvement exceeding 80% was observed in Figure 12(a). Although the solution can be further improved by using

the commercial Xsens IMU, the tightly coupled PPP/IMU fusion is shown to be beneficial by providing more accurate and resilient solutions in an obstructed environment. The use of the smartphone IMU is able to essentially mitigate the standalone PPP 2D RMS errors from 35.1 m to 6.6 m, with fewer than four visible satellites. The improvement decreased to approximately 10% in the scenarios in which the number of satellites was between five and seven, thus indicating lesser effects from using the IMU measurements when more satellites are available, in agreement with the conclusions in previous sections.

5 | CONCLUSION

The study provides insight into native smartphone PPP/IMU navigation performance by using current hardware and software platforms, with a focus on urban performance in the presence of obstructions. Compared with the GNSS/IMU integrated solution used in the past without PPP augmentation, the study represents a major step forward by investigating daily driving scenarios with an overall horizontal RMS of 2.1 m. In addition, in GNSS-denied underpasses, the integrated solution was able to provide a continuous smartphone navigation solution. The enhanced continuity is provided at no additional hardware cost, and should be beneficial in helping application developers improve their location-based services.

The answers to the key research questions that motivated this research are as follows, according to the experiments conducted:

1. How does the performance of a smartphone PPP/IMU integrated solution compare to that of a smartphone using an identical GNSS source but better IMUs?
   The tightly coupled solution improved after switching to a commercial low-cost IMU, wherein the overall RMS was improved from 2.1 m with the use of native sensors to 1.9 m. The commercial IMU showed much better performance in GNSS outages. Particularly in the second underpass, the Mi8/Xsens combination yielded a 1.2-m 2D RMS, as compared with 2.5 m with native sensors.
2. In what scenarios does a smartphone IMU improve navigation solutions, and by how much?
   The integrated solution using native sensors showed meters of improvement in overall accuracy. Notably, in GNSS outages, a 37% improvement was observed in the first outage, and an improvement from 15.7 m to 2.5 m was observed in the second outage. In scenarios with four or fewer satellites, the integrated solution provided a >80% improvement, covering 3.8% of the data set. A >10% improvement was observed with five to seven satellites; a 6% improvement was observed in more open-sky scenarios with more than seven satellites.

This study provides a more accurate and resilient positioning solution using current-generation smartphone sensors and a GNSS-PPP/IMU fusion technique. In the evolving industry of smartphone applications and portable devices, the improved solution should allow for better quality of services, such as more accurate delivery tracking in urban centers or improved navigation in obstructed areas. With the future development of a more resilient smartphone positioning solution, lane-level, all-around navigation, and more innovations are expected to be achieved.

6 | FUTURE WORK

The results demonstrated that the smartphone GNSS-PPP/IMU is capable of producing a consistent sub-meter-level navigation solution. However, the work must be extended to the realm of realistic scenarios in which phones are placed next to the driver, and the vehicle is traveling in a more complex and obstructed environment. Smartphone GNSS measurements show poor quality in both the RMS of larger errors and are also missing dual-frequency and carrier-phase measurements in some epochs. Therefore, further investigation and optimization are required. Additional algorithms to decouple the user's phone movement at hands and vehicular movement are needed to support practical use. The ultimate goal of this research is to produce a nearly ubiquitous, real-time sub-meter PNT solution available for smartphones that will lead to evolution of consumer technologies.

ACKNOWLEDGEMENTS

The authors thank the Natural Sciences and Engineering Research Council (NSERC) and York University for providing funding for this research, and the German Research Center for Geosciences (GFZ), International GNSS Services (IGS) and Centre National d'Etudes Spatiales (CNES), for data.

CONFLICTS OF INTEREST

The authors declare no potential conflicts of interest.

REFERENCES

Aggrey, J., Bisnath, S., Naciri, N., Shinghal, G., & Yang, S. (2020). Multi-GNSS precise point positioning with next-generation smartphone measurements. *Journal of Spatial Science, 65*(1), 79–98. https://doi.org/10.1080/14498596.2019.1664944

Banville, S., Lachapelle, G., Ghoddousi-Fard, R., & Gratton, P. (2019). Automated processing of low-cost GNSS receiver data. *Proc. of the 32nd International Technical Meeting of the Satellite Division of the Institute of Navigation (ION GNSS+ 2019),* Miami, FL, 3636–3652. https://doi.org/10.33012/2019.16972

Bilal, M. (2017). A review of internet of things architecture, technologies and analysis smartphone-based attacks against 3D printers. https://doi.org/10.48550/arXiv.1708.04560

Bisnath, S., & Gao, Y. (2009). Current state of precise point positioning and future prospects and limitations. In M. G. Sideris (Ed.), *Observing our changing earth* (pp. 615–623). Springer. https://doi.org/10.1007/978-3-540-85426-5_71

Cai, C., & Gao, Y. (2007). Precise point positioning using combined GPS and GLONASS observations. *Journal of Global Positioning Systems, 6*(1), 13–22. https://www.researchgate.net/publication/255604452_Precise_point_positioning_using_combined_GPS_and_GLONASS_observations

Dumitru, A. I., Girbacia, T., Boboc, R. G., Postelnicu, C. -C., & Mogan, G. -L. (2018). Effects of smartphone based advanced driver assistance system on distracted driving behavior: a simulator study. *Computers in Human Behavior, 83*, 1–7. https://doi.org/10.1016/j.chb.2018.01.011

Eckl, M. C., Snay, R. A., Soler, T., Cline, M. W., & Mader, G. L. (2001). Accuracy of GPS-derived relative positions as a function of interstation distance and observing-session duration. *Journal of Geodesy, 75*(12), 633–640. https://doi.org/10.1007/s001900100204

Eueler, H. -J., & Goad, C. C. (1991). On optimal filtering of GPS dual frequency observations without using orbit information. *Bulletin géodésique, 65*(2), 130–143. https://doi.org/10.1007/BF00806368

European Union Agency for the Space Programme (EUSPA). (2019). *GSA GNSS market report* (issue 6). https://www.euspa.europa.eu/system/files/reports/market_report_issue_6_v2.pdf

Farrell, J., & Barth, M. (1999). *The global positioning system and inertial navigation* (Vol. 61). McGraw-Hill.

Fortunato, M., Critchley-Marrows, J., Siutkowska, M., Ivanovici, M. L., Benedetti, E., & Roberts, W. (2019). Enabling high accuracy dynamic applications in urban environments using PPP and RTK on Android multi-frequency and multi-GNSS smartphones. *2019 European Navigation Conference (ENC)*, Warsaw, Poland. https://doi.org/10.1109/EURONAV.2019.8714140

Gao, Z., Ge, M., Shen, W., Zhang, H., & Niu, X. (2017). Ionospheric and receiver DCB-constrained multi-GNSS single-frequency PPP integrated with MEMS inertial measurements. *Journal of Geodesy, 91*(11), 1351–1366. https://doi.org/10.1007/s00190-017-1029-7

Ge, M., Zhang, H., Jia, X., Song, S., & Wickert, J. (2012). What is achievable with current COMPASS constellations? *Proc. of the 25th International Technical Meeting of the Satellite Division of the Institute of Navigation (ION GNSS 2012),* Nashville, TN, 331–339. https://www.ion.org/publications/abstract.cfm?articleID=10250

Gikas, V., & Perakis, H. (2016). Rigorous performance evaluation of smartphone GNSS/IMU sensors for ITS applications. *Sensors, 16*(8), 1240. https://doi.org/10.3390/s16081240

Godha, S. (2006). *Performance evaluation of low cost MEMS-based IMU integrated with GPS for land vehicle navigation application* (UCGE Report No. 20239). https://www.ucalgary.ca/engo_webdocs/MEC/06.20239.SGodha.pdf

Hernández-Pajares, M., Juan, J. M., Sanz, J., Orus, R., Garcia-Rigo, A., Feltens, J., Komjathy, A., Schaer, S. C., & Krankowski, A. (2009). The IGS VTEC maps: a reliable source of ionospheric information since 1998. *Journal of Geodesy, 83*(3-4), 263–275. https://doi.org/10.1007/s00190-008-0266-1

Humphreys, T. E., Murrian, M., van Diggelen, F., Podshivalov, S., & Pesyna, K. M. (2016). On the feasibility of cm-accurate positioning via a smartphone's antenna and GNSS chip. *2016 IEEE/ION Position, Location and Navigation Symposium (PLANS),* Savannah, GA. https://doi.org/10.1109/PLANS.2016.7479707

Kouba, J., & Héroux, P. (2001). Precise point positioning using IGS orbit and clock products. *GPS Solutions, 5*(2), 12–28. https://doi.org/10.1007/PL00012883

Li, G., & Geng, J. (2019). Characteristics of raw multi-GNSS measurement error from Google Android smart devices. *GPS Solutions, 23*(3), 90. https://doi.org/10.1007/s10291-019-0885-4

Liu, T., Yuan, Y., Zhang, B., Wang, N., Tan, B., & Chen, Y. (2017). Multi-GNSS precise point positioning (MGPPP) using raw observations. *Journal of Geodesy, 91*(3), 253–268. https://doi.org/10.1007/s00190-016-0960-3

Lou, Y., Zheng, F., Gu, S., Wang, C., Guo, H., & Feng, Y. (2016). Multi-GNSS precise point positioning with raw single-frequency and dual-frequency measurement models. *GPS Solutions, 20*(4), 849–862. https://doi.org/10.1007/s10291-015-0495-8

Nie, Z., Liu, F., & Gao, Y. (2020). Real-time precise point positioning with a low-cost dual-frequency GNSS device. *GPS Solutions, 24*(1), 9. https://doi.org/10.1007/s10291-019-0922-3

Øvstedal, O. (2002). Absolute positioning with single-frequency GPS receivers. *GPS Solutions, 5*(4), 33–44. https://doi.org/10.1007/PL00012910

Paziewski, J. (2020). Recent advances and perspectives for positioning and applications with smartphone GNSS observations. *Measurement Science and Technology, 31*(9), 091001. https://doi.org/10.1088/1361-6501/ab8a7d

Robustelli, U., Baiocchi, V., & Pugliano, G. (2019). Assessment of dual frequency GNSS observations from a Xiaomi Mi 8 Android smartphone and positioning performance analysis. *Electronics, 8*(1), 91. https://doi.org/10.3390/electronics8010091

Schaer, S., Gurtner, W., & Feltens, J. (1998). IONEX: the ionosphere map exchange format version 1.1. *Proc. of the IGS AC Workshop,* Darmstadt, Germany. http://ftp.aiub.unibe.ch/ionex/draft/ionex11.pdf

Shi, C., Gu, S., Lou, Y., & Ge, M. (2012). An improved approach to model ionospheric delays for single-frequency precise point positioning. *Advances in Space Research, 49*(12), 1698–1708. https://doi.org/10.1016/j.asr.2012.03.016

Shinghal, G., & Bisnath, S. (2020). Analysis and pre-processing of raw measurements from smartphones in realistic environments. *Proc. of the 33rd International Technical Meeting of the Satellite Division of the Institute of Navigation (ION GNSS+ 2020)*, 3140– 3154. https://doi.org/10.33012/2020.17709

Shinghal, G., & Bisnath, S. (2021). Conditioning and PPP processing of smartphone GNSS measurements in realistic environments. *Satellite Navigation, 2*(1), 10. https://doi.org/10.1186/s43020-021-00042-2

Sunkevic, M. (2017). Using GNSS raw measurements on Android devices [Tutorial Part I]. https://ipin2018.ifsttar.fr/fileadmin/contributeurs/IPIN2018/Tutorials/Using_GNSS_Raw_Measurements_on_Android_Devices_-_IPIN_2018_Tutorial_FV.pdf.

Tu, R., Ge, M., Zhang, H., & Huang, G. (2013). The realization and convergence analysis of combined PPP based on raw observation. *Advances in Space Research, 52*(1), 211–221. https://doi.org/10.1016/j.asr.2013.03.005

Vana, S., Naciri, N., & Bisnath, S. (2019). Low-cost, dual-frequency PPP GNSS and MEMS-IMU integration performance in obstructed environments. *Proc. of the 32nd International Technical Meeting of the Satellite Division of the Institute of Navigation (ION GNSS+ 2019),* Miami, FL, 3005–3018. https://doi.org/10.33012/2019.16966

Wang, L., Li, Z., Wang, N., & Wang, Z. (2021). Real-time GNSS precise point positioning for low-cost smart devices. *GPS Solutions, 25*(2), 69. https://doi.org/10.1007/s10291-021-01106-1

Xiang, Y., & Gao, Y. (2017). Improving DCB estimation using uncombined PPP. *NAVIGATION, 64*(4), 463–473. https://doi.org/10.1002/navi.207

Xiang, Y., Gao, Y., & Li, Y. (2017). Ionospheric STEC and VTEC constraints for fast PPP. In J. Sun, J. Liu, Y. Yang, S. Fan, & W. Yu (Eds.), *China Satellite Navigation Conference (CSNC): 2017 Proc. Vol. II* (pp. 257–269). https://doi.org/10.1007/978-981-10-4591-2_21

Yan, W., Bastos, L., & Magalhães, A. (2019). Performance assessment of the Android smartphone's IMU in a GNSS/INS coupled navigation model. *IEEE Access, 7,* 171073–171083. https://doi.org/10.1109/ACCESS.2019.2956239

Yan, W., Zhang, Q., Wang, L., Mao, Y., Wang, A., & Zhao, C. (2020). A modified Kalman filter for integrating the different rate data of gyros and accelerometers retrieved from Android smartphones in the GNSS/IMU coupled navigation. *Sensors, 20*(18), 5208. https://doi.org/10.3390/s20185208

Yang, L., Li, Y., Wu, Y., & Rizos, C. (2014). An enhanced MEMS-INS/GNSS integrated system with fault detection and exclusion capability for land vehicle navigation in urban areas. *GPS Solutions, 18*(4), 593–603. https://doi.org/10.1007/s10291-013-0357-1

Yi, D., Bisnath, S., Naciri, N., & Vana, S. (2021). Effects of ionospheric constraints in precise point positioning processing of geodetic, low-cost and smartphone GNSS measurements. *Measurement, 183,* 109887. https://doi.org/10.1016/j.measurement.2021.109887

Zhang, H., Gao, Z., Ge, M., Niu, X., Huang, L., Tu, R., & Li, X. (2013). On the convergence of ionospheric constrained precise point positioning (IC-PPP) based on undifferential uncombined raw GNSS observations. *Sensors, 13*(11), 15708–15725. https://doi.org/10.3390/s131115708

Zhang, X., Tao, X., Zhu, F., Shi, X., & Wang, F. (2018). Quality assessment of GNSS observations from an Android N smartphone and positioning performance analysis using time-differenced filtering approach. *GPS Solutions, 22*(3), 70. https://doi.org/10.1007/s10291-018-0736-8

Zhao, J., Hernández-Pajares, M., Li, Z., Wang, N., & Yuan, H. (2021). Integrity investigation of global ionospheric TEC maps for high-precision positioning. *Journal of Geodesy, 95*(3), 35. https://doi.org/10.1007/s00190-021-01487-8

Zumberge, J. F., Heflin, M. B., Jefferson, D. C., Watkins, M. M., & Webb, F. H. (1997). Precise point positioning for the efficient and robust analysis of GPS data from large networks. *Journal of Geophysical Research: Solid Earth, 102*(B3), 5005–5017. https://doi.org/10.1029/96JB03860

How to cite this article: Yang, S., Yi, D., Vana, S., & Bisnath, S. (2023). Resilient smartphone positioning using native and PPP augmentation. *NAVIGATION*, *70*(2). https://doi.org/10.33012/navi.567